J Mater Sci (2017) 52:478–488

Sustainable activated carbon fiber from sawdust by reactivation for high-performance supercapacitors

Yuxiang Huang[1,2], Yue Liu[2], Guangjie Zhao[1,*], and Jonathan Y. Chen[2,*]

[1] College of Materials Science and Technology, Beijing Forestry University, Tsinghua East Road 35, Haidian 100083, Beijing, China
[2] School of Human Ecology, The University of Texas at Austin, Austin, TX 78712, USA

Received: 28 July 2016
Accepted: 26 August 2016
Published online: 4 October 2016

ABSTRACT

Activated carbon fibers (ACFs) produced from recycled fir sawdust were used as electrodes in supercapacitors. It was shown that the ultramicropores (0.65–0.85 nm) were most efficient in contributing to the supercapacitor capacitance, while mesopores helped increase the rate performance capacitance. The experimental ACF electrode supercapacitor indicated a capacitance of 242 F g^{-1} in 6 M KOH aqueous electrolyte exhibiting a high energy density of 8.4 Wh kg^{-1} at a power density of 250 W kg^{-1}. Excellent cycle stability was also achieved, showing a good competitiveness of wood-based ACFs in comparison with other activated carbons currently used in supercapacitors.

Introduction

Sawdust, as a type of lignocellulosic biomass, is a by-product from mechanical milling or processing of wood with various useable sizes [1], which can account for up to 20 % of the total input mass [2]. Currently, most of this wood waste is burnt directly for energy recovery, while a small proportion is land-filled, resulting in air pollution and occupation of useful land. Thus, increasing attention has been paid to the disposal of sawdust. Sawdust is usually used as a powder for mineral-bonded composites [3], filler of polymers [4], or chemical intermediates [5]. Besides, the use of lignocellulosic sawdust for the production of low-cost activated carbon materials is another popular approach due to its high carbonaceous content [6].

Activated carbons (ACs) are widely used in many fields such as adsorption and filtration due to abundantly developed pore structure and special surface reactivity. Most recently, one of the most important AC applications in the field of energy storage is supercapacitors [7], in which the charge accumulates at the electrode/electrolyte interface. High power density, long cycling durability, and rapid charge/discharge rate made supercapacitors an important device in complementing or replacing batteries in the field of energy storage [8]. Because pore size distribution (PSD) determines the moving ability of electrolyte ions, it has a great effect on the performance of supercapacitors. For ACs, the PSD range is 0.4–4 nm, which is too wide to render high capacitance. Therefore, activated carbons in the fiber form, called activated carbon fibers (ACFs) in which pore diameter and pore length could be easily controlled, have become competitive candidates for electrochemical applications [7].

Address correspondence to E-mail: zhaows@bjfu.edu.cn; jychen2@austin.utexas.edu

DOI 10.1007/s10853-016-0347-0

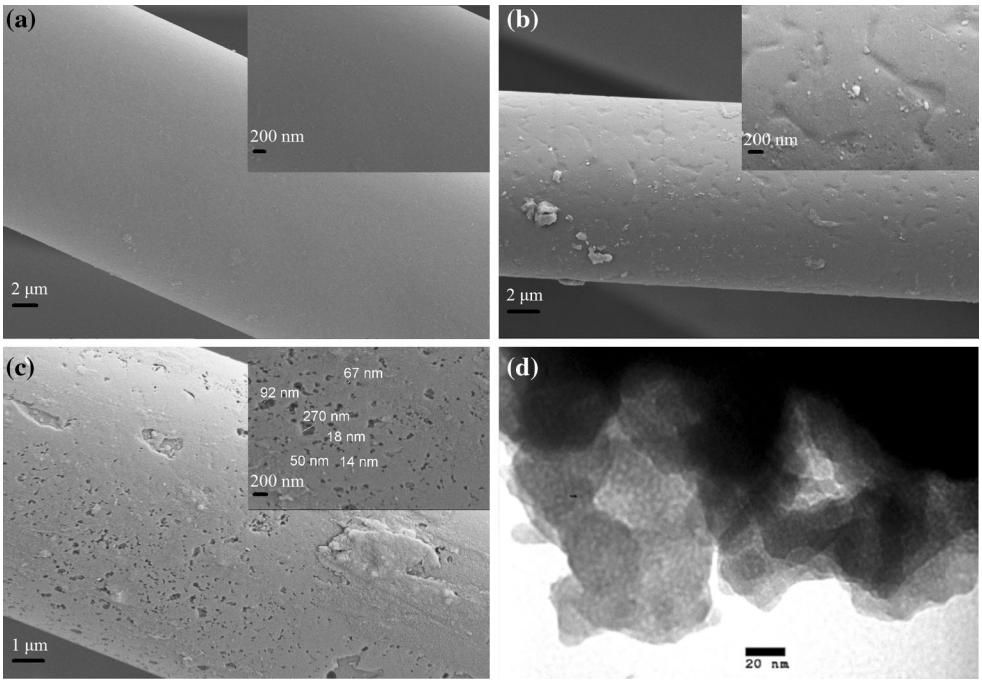

Figure 1 SEM images of AS **a**, AS750 **b**, and AS850-3 **c** and TEM image of AS850-3.

However, higher cost of ACFs becomes a barrier to quickly delivering ACF-based supercapacitors to marketplace [9]. It is very desirable to look for lower-cost carbons and much attention has been paid to lignocellulosic biomass [10–14]. Previous studies have shown that highly porous ACFs could be economically produced from sawdust via liquefaction technique, melt spinning, and electrospinning [15–21]. The resulted ACFs by steam or KOH activation have been used successfully for the removal of dye from wastewater [22]. However, either steam or KOH single activation mainly developed microporosity, which may not be effective for the electroadsorption of hydrated ions as ACFs were used as electrodes [23]. Reactivation, a combination of physical and chemical activation, could be an effective way to develop mesoporosity [24].

In an effort to further increase the profitability of using this abundantly available fir sawdust biomass, a study was conducted on the electrochemical behavior of the physicochemically reactivated ACFs as electrodes in a double-layer supercapacitor. Different reactivation conditions were exploited in order to obtain ACFs with different pore structures, which showed a significant influence on the supercapacitor's capacitance.

Materials and methods

Materials

The sawdust originated from Chinese fir (*Cunninghamia lanceolata*) was obtained from a furniture factory (Beijing, China). Phenol (C_6H_5OH), phosphoric acid (H_3PO_4, 37 wt%), hexamethylenetetramine ($C_6H_{12}N_4$), hydrochloric acid (HCl, 37 wt %), formaldehyde (CH_2O, 37 wt%), and potassium hydroxide (KOH) were purchased from Beijing Chemical Works. Polytetrafluorethylene (PTFE) and Super-P (SP) were purchased from Fisher Scientific. All the chemicals were of reagent grade and used without further purification.

Synthesis of activated carbon fibers

The sawdust was firstly pulverized and screened to a particle size of 60–80 meshes to prepare the precursor fibers through a series of processes including liquefaction, melt spinning, and curing according to our previous study [17]. The precursor fibers were put in a tube furnace and the activation process was carried out at 850 °C under steam–nitrogen gas mixture for 1 h. These steam-activated ACFs were labeled as AS.

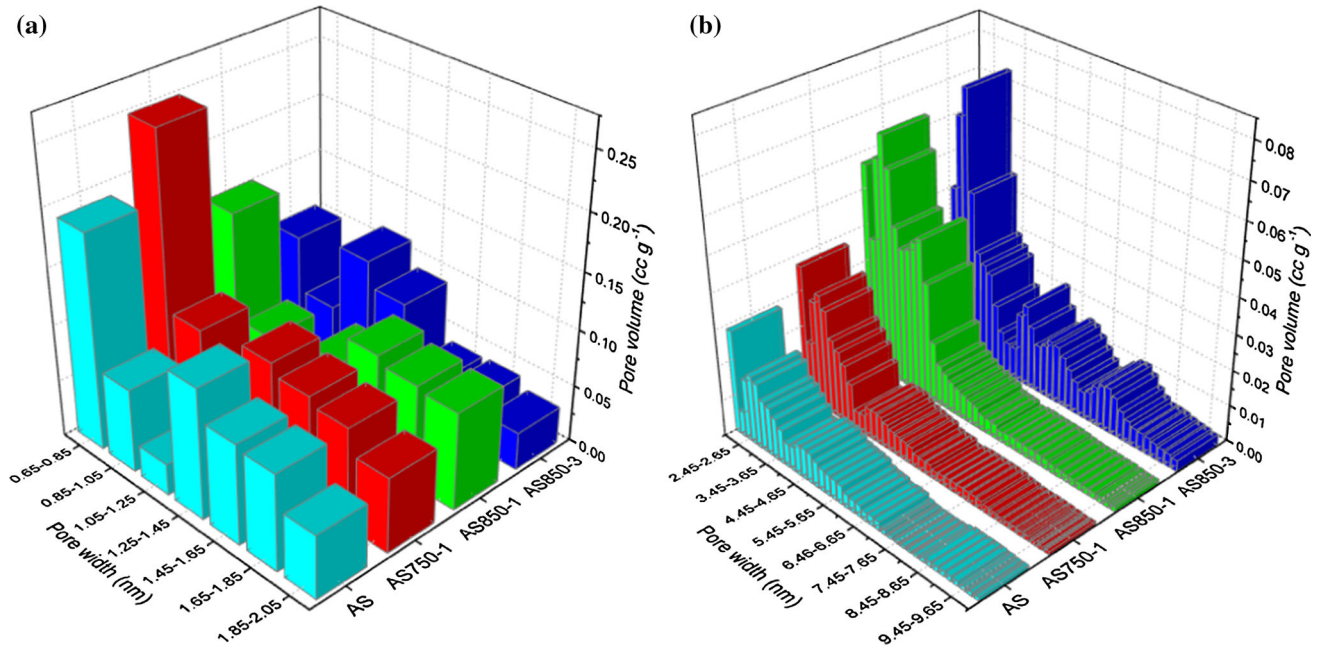

Figure 2 Pore volume *histogram* of ACF with different pore size region: **a** 0.65–2.05 nm and **b** 2.25–10.05 nm.

During the impregnation of AS, 30 % wt of KOH aqueous solution was brought into contact with the fibers, where KOH/fiber ratio was 6:1. The KOH-impregnated AS were then put in a horizontal transparent tube furnace (Y02B, Thermcraft Inc., USA) and heated to specified temperature under nitrogen flow at a heating rate of 4 °C min^{-1}. The as-prepared ACFs were denoted as AS*T*-*t*, where *T* (750 and 850) and *t* (1 and 3) represent the activation temperature (°C) and activation time (h), respectively.

Preparation of supercapacitors

A mixture of 83 wt% ACF, 10 wt% SP, and 7 wt% PTFE binder was homogenized in an agate mortar, formed into electrodes by rolling into 80-μm-thick sheets, and finally 7.5-mm-diameter disks were punched out of the sheets, followed by drying under vacuum at 100 °C for 12 h. The two-electrode test cell was assembled using carbon paper as two current collectors, the Whatman glassy fiber as a separator, and 6 M KOH aqueous solution as an electrolyte.

Characterization and electrical measurement

Surface morphology of the ACFs was examined via a scanning electron microscope (SEM) (Supra 40, Zeiss, Germany). Transmission electron microscopy (TEM) images were obtained using a JEOL JEM-1010 microscope operating at 79 kV. Nitrogen adsorption/desorption isotherms were collected at −196 °C on an Autosorb-iQ (Quantachrome) automatic analyzer. PSD data were obtained using the method of quenched solid density functional theory (QSDFT) based on the isotherm data. A micro-Raman spectrometer (RamanStation 400, PerkinElmer, MA, USA) was used to investigate the conformational state of graphite in the ACFs. X-ray photoelectron spectroscopy (XPS) measurements were performed on an ESCALAB 250Xi spectrometer (Thermo Fisher Scientific) using a monochromated Al Kα X-ray ($hv = 1486.6$ eV) source. A nonlinear least-square curve-fitting program (XPSPEAK software, Version 4.1) was used for XPS spectral deconvolution. The surface hydrophobicity of the ACF electrodes was tested through a static contact angle measurement using a VCA Optima® system.

Cyclic voltammetry (CV) curves at various scan rates from 5 to 100 mV s^{-1} and galvanostatic charge/discharge curves at different current densities from 0.5 to 10 A g^{-1} were measured using a potentiostat Eco Chemie Autolab PGSTA 100 equipped with the FRA2 frequency response analyzer module and GPES/FRA software. The capacitance was determined by the galvanostatic charge/discharge using $C = I/(dV/dt)$ with dV/dt calculated from the slope

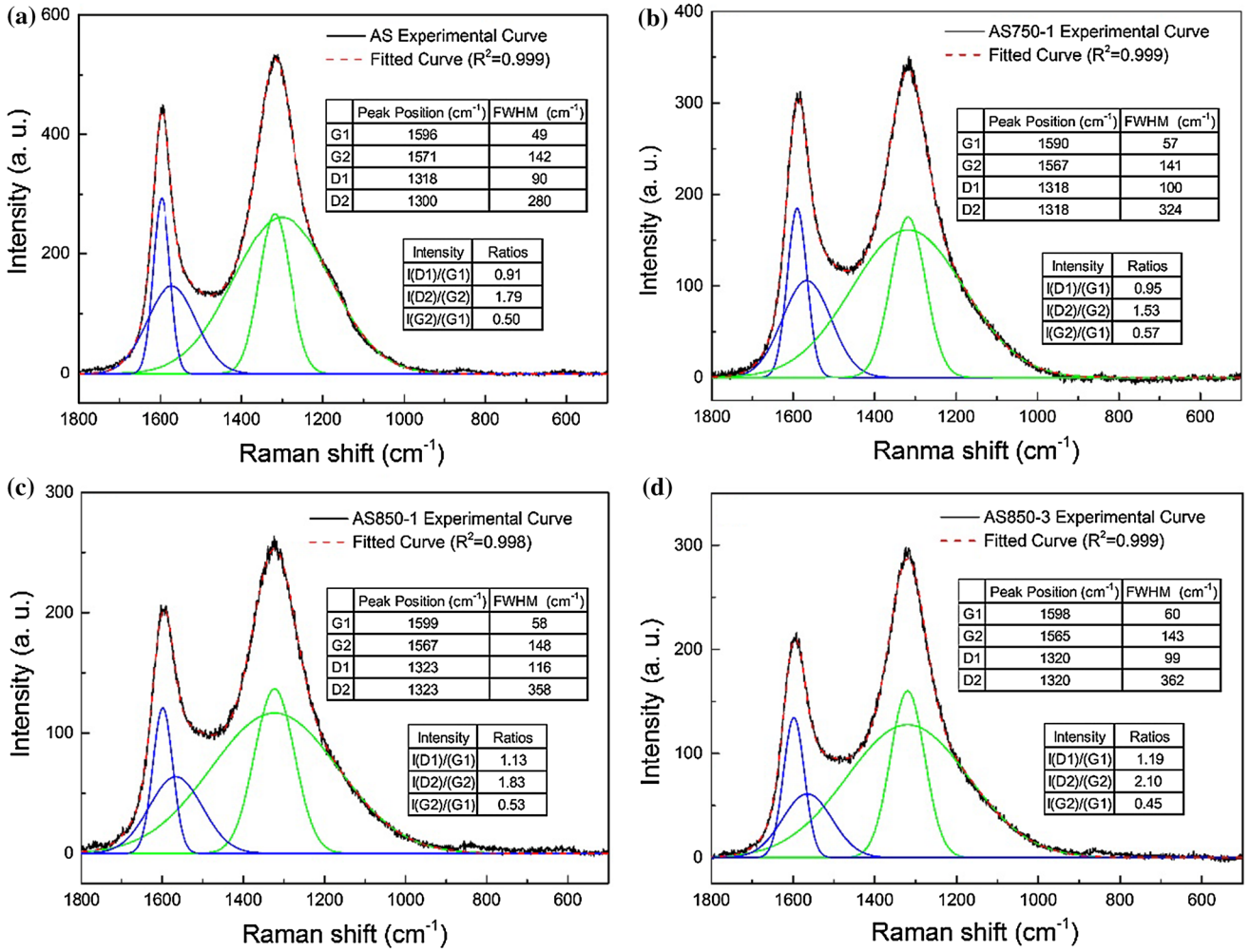

Figure 3 Raman spectra of steam-activated and KOH-reactivated ACFs with fitting results using four Gaussians: **a** AS, **b** AS750-1, **c** AS850-1, and **d** AS850-3.

of the discharge curves. The specific capacitance C_{sp}, defined as the capacitance per unit mass for one electrode, was calculated according to $C_{sp}(\mathrm{F\ g^{-1}}) = 4 \times C/m$, where m is the total mass of the active material in both electrodes. Energy density and power density were, respectively, calculated using $E = C_{sp}(\Delta V)^2/8$ and $P = E/\Delta t$, where ΔV is the voltage difference (obtained from the discharge curve subtracted by IR drop) and Δt is the discharge time.

Results and discussion

Morphological properties

Figure 1a–c shows the SEM micrographs of ACF samples. ACFs are composed of bundles of fibers with a diameter of about 11 μm. There is no significant shape difference between steam-activated ACFs (AS) and KOH-reactivated ACFs (AS750-1 and AS850-3). It is evident from Fig. 1a that the surface of AS is found to be smooth, whereas it is unable to judge the abundance of porosity. Commonly, the steam activation could develop the micropores (<2 nm) which cannot be observed in the SEM image due to the thin layer of Au and Pt (w/w 4) with a thickness of 12 nm metalized on the fiber. However, the KOH reactivation leads to notable surface roughness as seen in the inset of Fig. 1b, indicating that the surfaces were etched by the reaction between KOH and carbon. As the reactivation temperature was increased from 750 to 850 °C, the edges (including some already existing and newly created ones) were exposed to an attack perpendicular to the

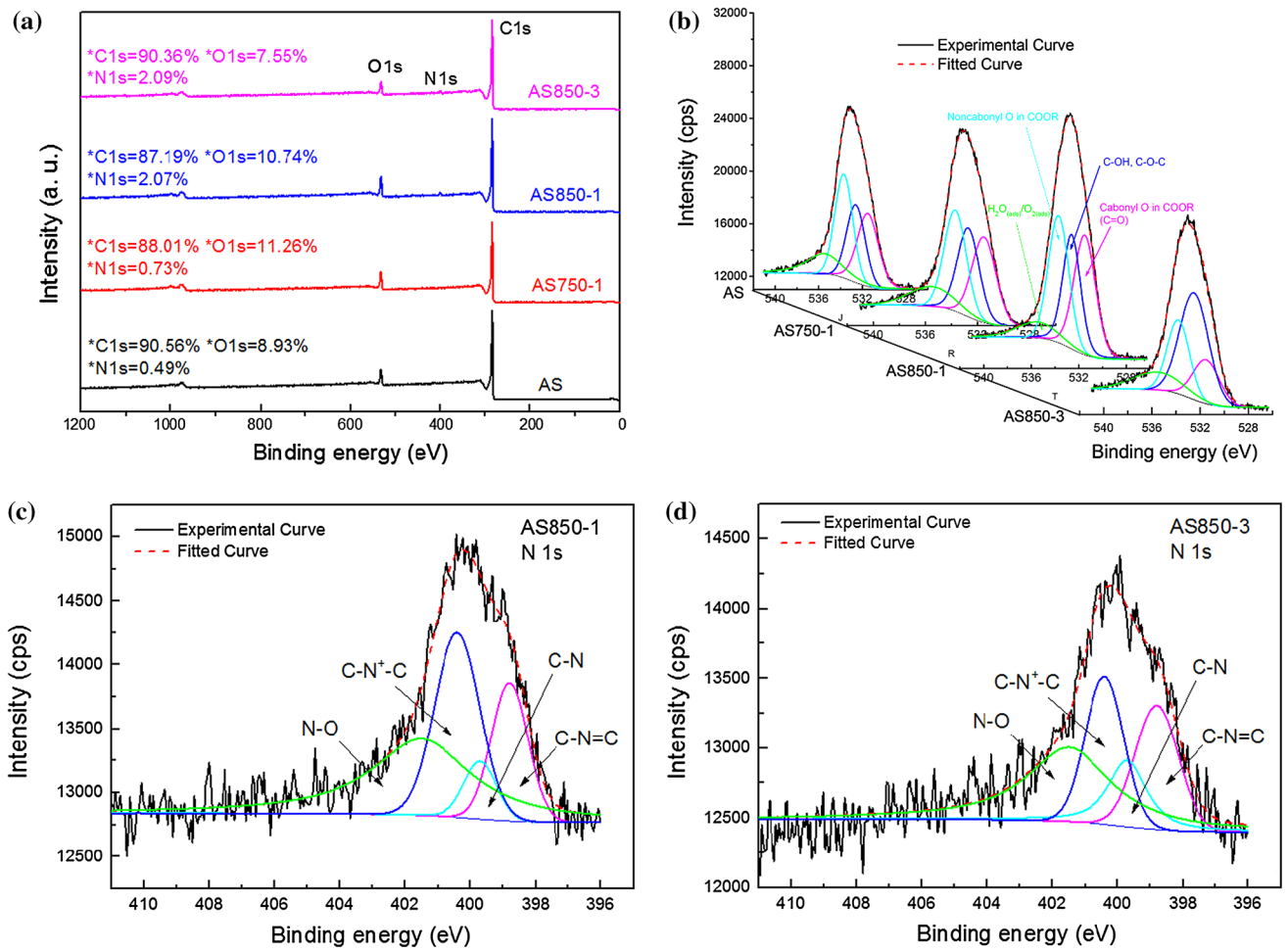

Figure 4 **a** XPS spectrum of steam-activated and KOH-reactivated ACFs with their C 1 s, O 1 s, and N 1 s % atomic concentrations (*asterisk*: atomic concentration); **b** curve-fitted high-resolution XPS for O 1 s and N 1 s for AS850-1 (**c**) and AS850-3 (**d**).

basal plane [25] and metallic K vapor exhibited an intercalation effect. As a result, AS850-1 has a rougher surface and more cavities than AS750-1. With prolonging the reactivation time, more nanoscale pores were generated on the surface of AS850-3 and small mesopores were embedded in the marcopores (the inset of Fig. 1c). This demonstrated that the KOH reactivation could be a valid method to develop the ACF mesoporosity. The TEM image again indicated that AS850-3 with porous texture has been successfully produced.

The parameters of porosity for those ACFs were described in our previous study in detail [26]. Figure 2 illustrates the pore volume histogram of the ACFs with different pore size regions. Apparently, AS750-1 has the most micropores distributed in the range of 0.65–0.85 nm (Fig. 2a), suggesting that the KOH reactivation at 750 °C was beneficial to the development of ultramicropores. When the reactivation temperature exceeded 800 °C, the mircopores were enlarged to small mesopores (2–10 nm) owing to more violent reactions between KOH and C as well as the intercalation effect of metallic K. This was reflected by the fact that the ultramicropores decreased sharply, while the mesopores within 2–10 nm increased significantly (Fig. 2b).

Graphitic characteristics

Figure 3 presents typical Raman spectra for the steam-activated and KOH-reactivated ACFs where broad and prominent G and D peaks can be found. The G band, in the range of 1600–1500 cm^{-1}, is ascribed to the Raman active E_{2g} in-plane vibration mode of carbons strongly coupled in the hexagonal sheets, while the D band in the 1400–1300 cm^{-1} range

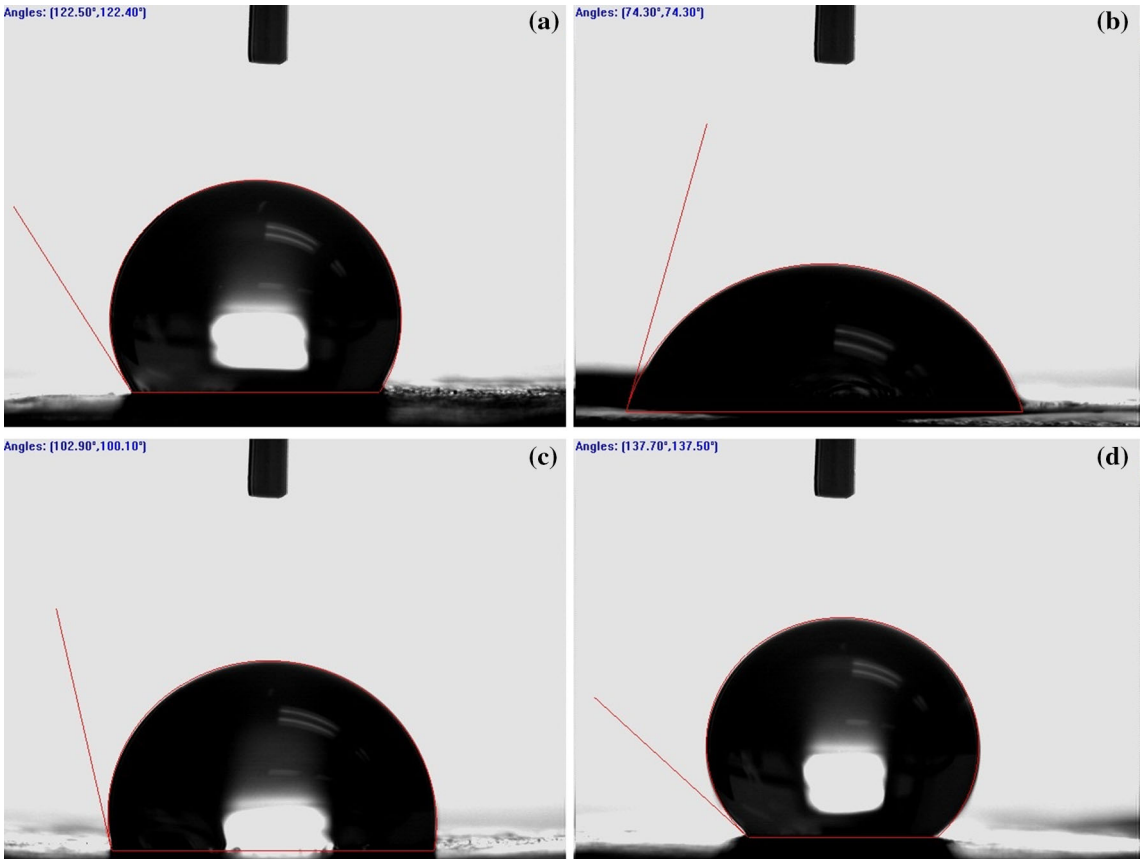

Figure 5 Contact angle measurement for all the ACF-based electrodes: **a** AS, **b** AS750-1, **c** AS850-1, and **d** AS850-3.

is assigned to A_{1g} mode similar to an in-plane breathing type [27]. The presence of the two bands, especially the D band, illustrates the ACFs of a highly disordered structure. The G and D bands exhibit asymmetric tailings, therefore they were further resolved into G1 & D1 and G2 & D2 peaks using the deconvolution technique proposed by Shimodaira and Masui to represent graphitic basal planes and sp^2 clusters [28].

As shown in Fig. 3, all the KOH-reactivated ACFs have larger full width at half maximum (FWHM) of G1 band than the steam-activated ACFs, indicating an increased bond disorder of the basal planes from the reactivation. The increase of FWHM of D2 band demonstrated that more defective species in the sp^2 clusters resulted from the reactivation, although the FWHM of the deconvoluted D2 band could be less accurate on account of the fitting method itself [29]. The I(D1)/I(G1) ratio, which was referred to be inversely proportional to the graphitization degree (in-plane crystalline size L_a), increased after the reactivation of AS. The ratio would continue to increase as the reactivation temperature goes up or the reactivation time prolongs. This suggested that the reactivation further would destroy the micro-crystallites to lower the graphitization degree. AS850-3 had the highest I(D2)/I(G2) ratio (proportional to the size of the part with bond angle disorder), indicating increased sizes of amorphous sp^2 carbon cluster from deep reactivation. However, the lowest I(G2)/I(G1) ratio for AS850-3 implied that the part with bond angle disorder was selectively removed or become ordered by deep reactivation [27].

Surface chemistry

Figure 4a shows the broad XPS spectra and atomic concentration of the surface of all the ACF samples. The liquefied wood-based ACFs were composed of the elements C, O, and N, which was confirmed by the peaks of C 1 s, O 1 s, and N 1 s in the range of 1200–0 eV binding energies. AS750-1 and AS850-1 had higher O contents than AS, indicating that the KOH reactivation increased the amount of surface

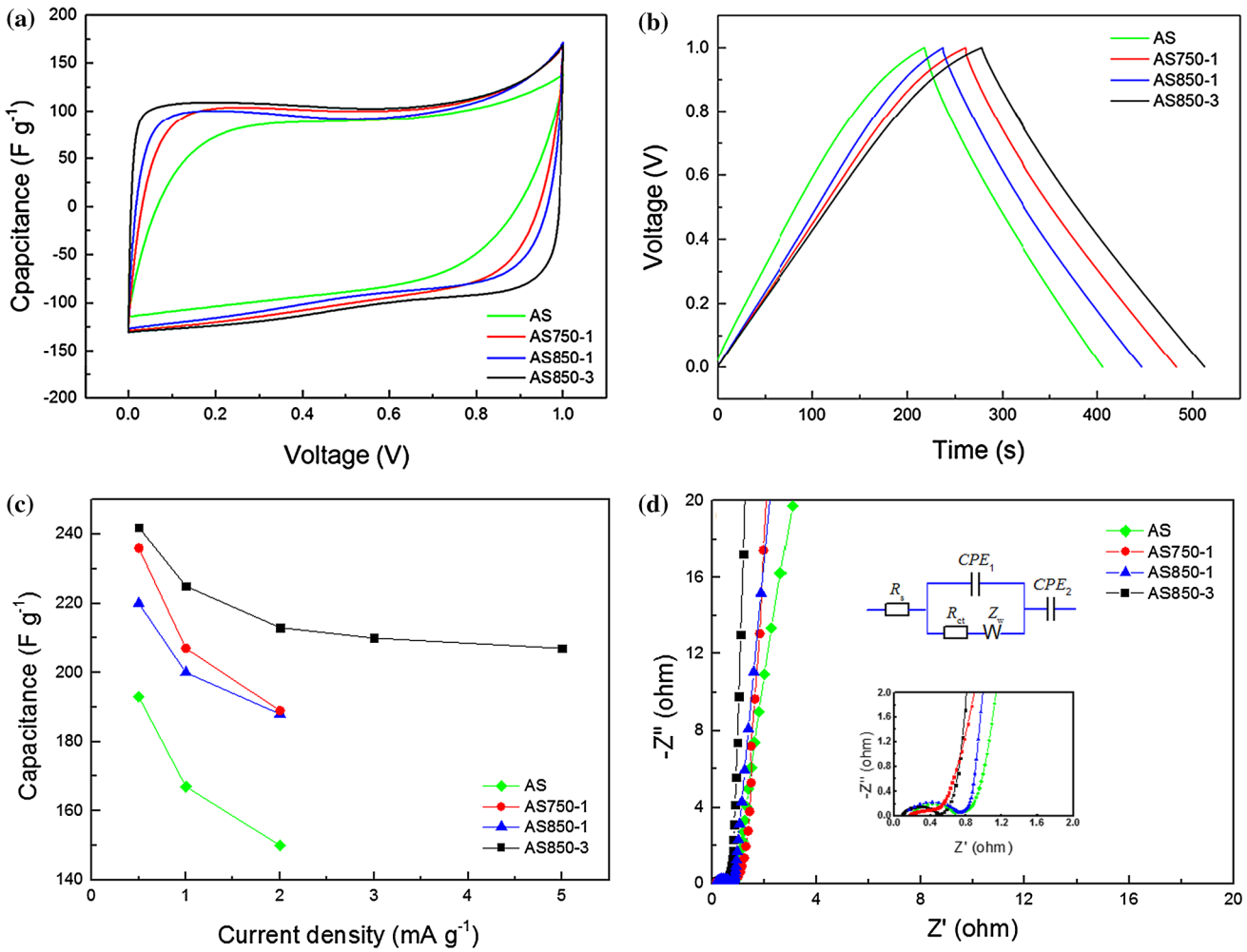

Figure 6 CV **a**, galvanostatic charge–discharge curves **b**, rate performance **c**, and Nyquist plots **d** of all the ACF-based supercapacitors.

oxides. However, deep reactivation consumed more O than C, causing the lowest O content (7.55 %) for AS850-3. Figure 4b shows the deconvolution of O1 s. The main O-containing functional groups of all the ACF samples were hydrophilic hydroxyl and carboxyl groups. Therefore, the lowest O content suggested that AS850-3 had high hydrophobicity, which was confirmed by the maximum contact angle of AS850-3 (Fig. 5). The varied trend of hydrophobicity was consistent with that of I(G2)/I(G1) ratio, suggesting that the deep reactivation consumed the disordered amorphous sp^2 carbon as well as the surface oxides to reduce polar groups, thereby increasing hydrophobicity of ACFs. It was reported that N-containing functional groups affected the electrochemical properties of the corresponding ACF-based supercapacitors [30]. So the deconvolution of N1 s for AS850-1 and AS850-3 is presented in Fig. 4c and 4d, respectively. Compared with AS850-1 (C–N 7.1 %, N–O 42.7 %), AS850-3 had a higher C–N bond content (14.5 %) and a lower N–O bond content (39.1 %), indicating that electrons would be transferred to the electrode more effectively for AS850-3.

Electrochemical performance

As shown in Fig. 6a, at the scan rate of 20 mV s^{-1} the CV curves of all the ACFs are almost rectangular, showing typical capacitive behavior of the ACF electrode. AS850-3 has the largest enclosed area, suggesting the highest capacitance. Calculated from the discharge curve (Fig. 6b), the specific capacitance values at 0.5 A g^{-1} for AS, AS750-1, AS850-1, and AS850-3 are 193, 236, 220, and 242 F g^{-1}, respectively. Figure 7a presents a similar variation trend of the specific capacitance to that of the specific surface

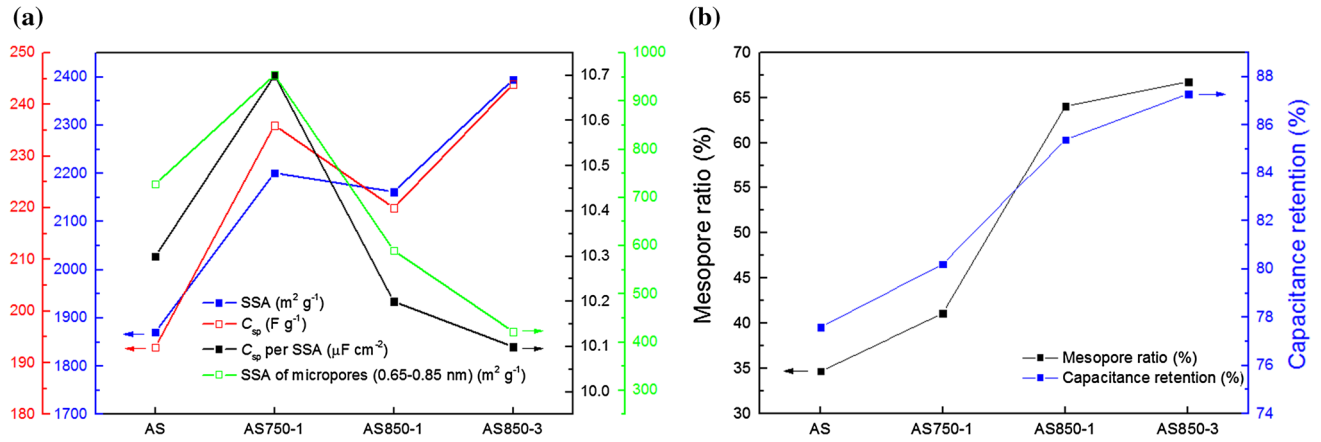

Figure 7 Variation trend of the specific surface area, specific capacitance, specific capacitance normalized by surface area, and specific surface area of utramicropores within 0.65–0.85 nm for different ACF samples **a** and the relationship between the mesopore ratio and capacitance retention **b**.

area. The ACF sample with the highest specific surface area (AS850-3) had the highest specific capacitance, confirming that the surface area is very important for electrode materials to accumulate charges. Figure 6c shows the rate performance of steam-activated and KOH-reactivated ACFs. The specific capacitance of all the ACF samples decreases with increasing current densities because the electrolyte ions did not have enough time to move into the narrow pores to form an electrochemical double layer when a higher scan rate for the charge and discharge was used. However, AS850-1, which had a lower specific capacitance than AS750-1 at 0.5 A g^{-1}, had the similar specific capacitance with AS750-1 at 2 A g^{-1}, showing that the mesoporous material had better rate performance. Figure 6d shows Nyquist plots of the ACF-based electrodes over the frequency range of 0.01–100 kHz, in which the linearity at low frequency was indicative of ideal capacitive behavior [31]. The slope of 45° region of the plots that represents the Warburg resistance (Z_w, 0.21–0.43Ω) was very short, demonstrating an efficient access of the electrolyte ions to the electrode surface. The semicircles in the high-frequency region with small diameters indicated very small charge transfer resistance (R_{ct}, 0.34–0.72 Ω). The real axis intercept in the high-frequency region also suggested a small equivalent serial internal resistance (R_s, 0.09–0.19 Ω).

In order to illustrate the effects of porosity on the specific capacitance of the ACF-based supercapacitors, specific surface area, specific capacitance, and normalized capacitance by the specific surface area at 0.5 A g^{-1} are plotted as a function of samples in Fig. 7a. The irregular variation of the normalized capacitance by the specific surface area suggests that there is no clear correlation between the specific surface area and the specific capacitance. AS750-1, which had the most accumulated pore volume within 0.65–0.85 nm (Fig. 2a), had the highest capacitance per surface area (10.7 μF cm^{-2}). AS850-1, which was mainly mesoporous, had lower capacitance per surface area although its specific surface area was similar to that of AS750-1. Therefore, the specific surface area of the micropores within 0.65–0.85 nm for the different ACF samples was also plotted in contrast to the normalized capacitance to see the effect of pore size. Their consistent variation trend indicates that the specific surface area of ultramicropores rather than mesopores is proportional to the supercapacitor's normalized capacitance. The effect of the mesopore ratio (mesopore volume/total pore volume) on the rate capability of the ACF samples is shown in Fig. 7b. The ACF within large mesopore ratio exhibits better rate performance, confirming that the mesopore structure offers better accessibility to electrolyte ions to achieve high capacitive performance at fast charge and discharge rates.

Figure 8a shows the CV curves of AS850-3 at different scan rates. Even at a high scan rate of 100 mV s^{-1}, the curve still maintains the rectangular shape rather than spindle shape. Correspondingly, the GC curves (Fig. 8b) are always symmetric triangle shaped no matter at low or high current densities, except that the voltage drops at the beginning of the discharge process become large with the increasing current densities. Simultaneously, the good linear relation of potentials vs. time suggests a rapid I–V response and excellent capacitive performance [32].

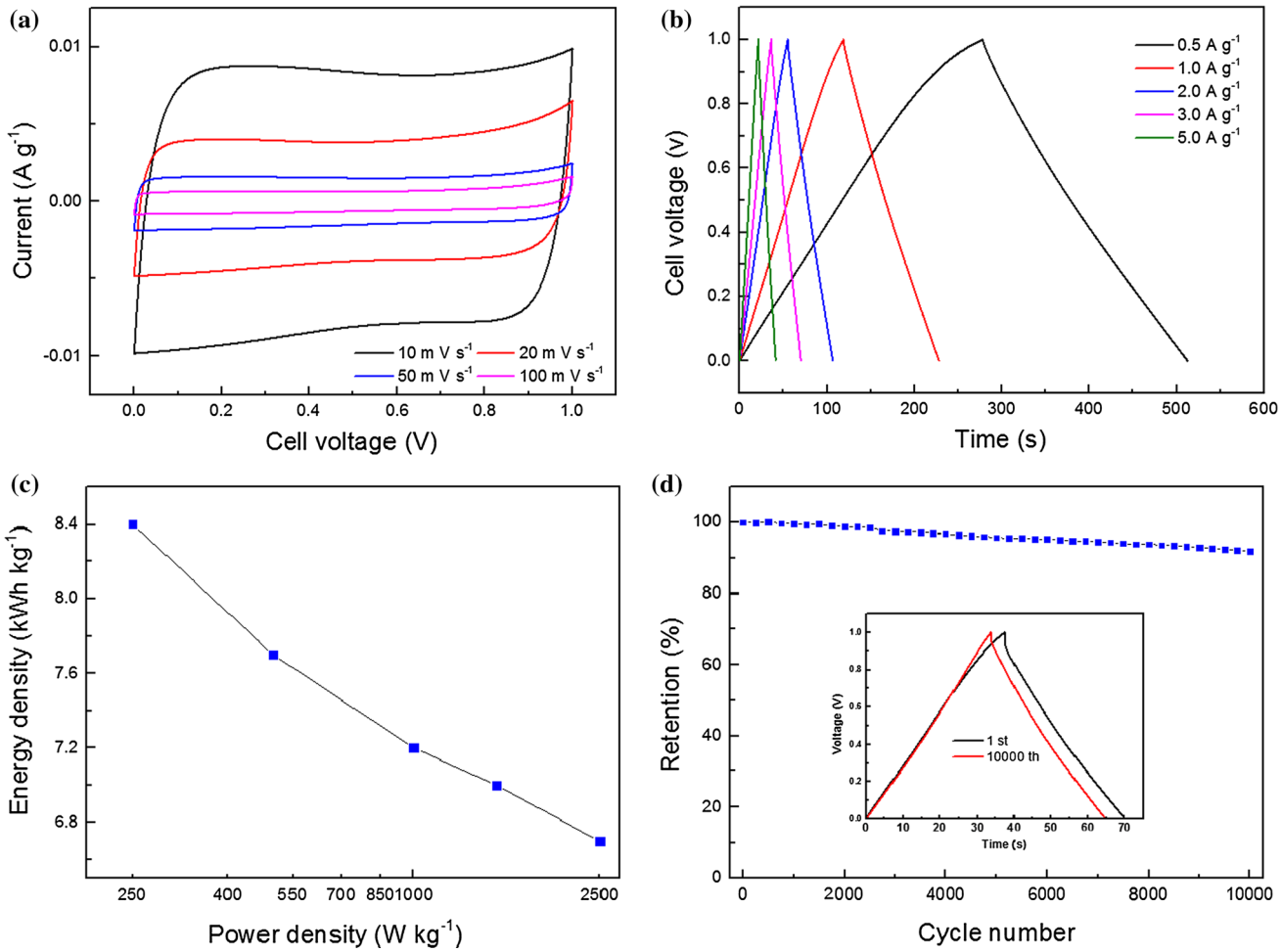

Figure 8 Electrochemical performance of the AS850-3 electrode: **a** CV curves at different scan rates from 10 to 100 mV s^{-1}, **b** galvanostatic charge–discharge curves at different current densities from 0.5 to 10 A g^{-1}, **c** energy and power density, and **d** cycle performance at a current density of 3 A g^{-1}.

Calculated from the charge curve, AS850-3 had an energy density of 8.4 Wh kg^{-1} at a power density of 250 W kg^{-1}. It can retain an energy density of 6.7 Wh kg^{-1} at a higher power density of 2.5 kW kg^{-1} (F). These energy densities are higher than those of many reported activated carbon-based supercapacitors from biomass materials, such as 2.63 Wh kg^{-1} for rubber wood sawdust at 291 W kg^{-1} [33] and 1–2 Wh kg^{-1} for coconut shell at 4.5 kWkg^{-1} [12]. Furthermore, the cycling stability of AS850 electrode, which was also a very important parameter, was evaluated by galvanostatic charge–discharge for 10000 cycles. Figure 8d shows the specific capacitance of AS850-3 electrode as a function of cycle number at a current density of 3 A g^{-1}. This electrode exhibits excellent cycling stability with 91.8 % capacitance retention after 10000 cycles.

Conclusion

The ACFs produced from fir sawdust exhibited a great feasibility as electrode materials for high-performance supercapacitors. The method of steam–KOH reactivation for the fir sawdust ACFs has proved to be an effective process to produce highly porous ACFs. Different porous structures of ACF could be obtained by controlling the reactivation temperature. Micropores within 0.65–0.85 nm mostly contributed to the electric double-layer capacitance and mesopores were responsible for the good rate performance. The mesoporous ACFs with the highest specific surface area (2395 m^2 g^{-1}) could achieve a high capacitance of 242 F g^{-1} at a low current density of 0.5 A g-1 in the 6 M KOH aqueous electrolyte. At a power density of 250 W kg^{-1}, the energy density

reached 8.4 Wh kg^{-1}. The supercapacitor was able to retain 80 % of energy density at 2.5 kW kg^{-1}. The ACF electrode also showed an excellent cycle stability with 91.8 % coulombic efficiency at 3 A g^{-1} after 10000 cycles.

Acknowledgements

The authors gratefully acknowledge the financial support from the China National Science & Technology Pillar Program through the Project "Key technology and application demonstration for the production of wood-based functional adsorption materials" (2015BAD14B06) and from China Scholarship Council. Thanks are also extended to Dr. Mourad Krifa and Mr. Hao Wu in the School of Human Ecology at The University of Texas at Austin for their help with the contact angle test and Dr. Guihua Yu and Mr. Lele Peng in the Materials Science and Engineering Program and Department of Mechanical Engineering at The University of Texas at Austin for their help with electrochemical test.

References

[1] Dai D, Fan M (2005) Preparation of bio-composite from wood sawdust and gypsum. Ind Crop Prod 74:417–424

[2] Gan Q, Allen SJ, Matthews R (2004) Activation of waste MDF sawdust charcoal and its reactive dye adsorption characteristics. Waste Manag 24:841–848

[3] Paramasivam P, Loke YO (1980) Study of sawdust concrete. Int J Cem Compos Lightweight Concrete 2:57–61

[4] Falcão L, Araújo MEM (2014) Application of ATR-FTIR spectroscopy to the analysis of tannins in historic leathers: the case study of the upholstery from the 19th century Portuguese royal train. Vib Spectrosc 74:98–103

[5] Tymchyshyn M, Xu CC (2010) Liquefaction of bio-mass in hot-compressed water for the production of phenolic compounds. Bioresour Technol 101:2483–2490

[6] Foo KY, Hameed BH (2012) Mesoporous activated carbon from wood sawdust by K_2CO_3 activation using microwave heating. Bioresour Technol 111:425–432

[7] Pandolfo AG, Hollenkamp AF (2006) Carbon properties and their role in supercapacitors. J Power Sources 157:11–27

[8] Simon P, Gogotsi Y (2008) Materials for electrochemical capacitors. Nat Mater 7:845–854

[9] Burke A (2007) R&D considerations for the performance and application of electrochemical capacitors. Electrochim Acta 53:1083–1091

[10] Hu S, Zhang S, Pan N, Hsieh Y (2014) High energy density supercapacitors from lignin derived submicron activated carbon fibers in aqueous electrolytes. J Power Sources 270:106–112

[11] Ruiz-Fernández M, Alexandre-Franco M, Fernández-González C, Gómez-Serrano V (2011) Development of activated carbon from vine shoots by physical and chemical activation methods. Some insight into activation mechanisms, Adsorption 17:621–629

[12] Olivares-Marín M, Fernández JA, Lázaro MJ, Fernández-González C, Macías-García A, Gómez-Serrano V, Stoeckli F, Centeno TA (2009) Cherry stones as precursor of activated carbons for supercapacitors. Mater Chem Phys 114:323–327

[13] Xie L, Sun G, Su F (2016) Hierarchical porous carbon microtubes derived from willow catkins for supercapacitor applications. J Mater Chem A 4:1637–1646

[14] Feng H, Zheng M, Dong H (2015) Three-dimensional honeycomb-like hierarchically structured carbon for high-performance supercapacitors derived from high-ash-content sewage sludge. J Mater Chem A 3:15225–15234

[15] Alma MH, Yoshioka M, Yao Y, Shiraishi N (1996) Preparation and characterization of the phenolated wood using hydrochloric acid (HCl) as a catalyst, Wood Sci. Technol. 30:39–47

[16] Alma MH, Yoshioka M, Yao Y, Shiraishi N (1995) Preparation of oxalic acid-catalyzed resinified phenloated wood and its characterization. Mokuzai Gakkaishi 41:1122–1131

[17] Liu W, Zhao G (2012) Effect of temperature and time on microstructure and surface functional groups of activated carbon fibers prepared from liquefied wood. BioResources 4:5552–5567

[18] Huang Y, Zhao G (2015) Preparation and characterization of activated carbon fibers from liquefied wood by KOH activation. Holzforschung 70:195–202

[19] Huang Y, Ma E, Zhao G (2015) Thermal and structure analysis on reaction mechanisms during the preparation of activated carbon fibers by KOH activation from liquefied wood-based fibers. Ind Crop Prod 69:447–455

[20] Huang Y, Peng L, Liu Y, Zhao G, Chen JY, Yu G (2016) Biobased nano porous active carbon fibers for high-performance supercapacitors, ACS Appl. Mater. Inter. 8:15205–15215

[21] Tian Z, Zhang W, Lu W (2016) Preparation of nanofibers from phenol liquefied wood by electrospinning. Nanomater, Nanotechno

[22] Huang Y, Ma E, Zhao G (2015) Preparation of liquefied wood-based activated carbon fibers by different activation methods for methylene blue adsorption. RSC Adv 5:70287–70296

[23] Shi H (1996) Activated carbons and double layer capacitance. Electrochim Acta 41:1633–1639

[24] Miyamoto J, Kanoh H, Kaneko K (2005) The addition of mesoporosity to activated carbon fibers by a simple reactivation process. Carbon 43:855–857

[25] Xue R, Yan J, Liu X, Yi Y, Tian B (2011) Effect of activation on the carbon fibers from phenol-formaldehyde resins for electrochemical supercapacitors. J Appl Electrochem 41:1357–1366

[26] Huang Y, Zhao G (2016) A novel method for the production of mesoporous activated carbon fibers from liquefied wood. Mater Lett 178:90–92

[27] Zhao Y, Fang F, Xiao H, Feng W, Xiong L, Fu S (2015) Preparation of pore-size controllable activated carbon fibers from bamboo fibers with superior performance for xenon storage. Chem Eng J 270:528–534

[28] Shimodaira N, Masui A (2002) Raman spectroscopic investigations of activated carbon materials. J Appl Phys 92:902–909

[29] Hu S, Hsieh Y (2014) Preparation of activated carbon and silica particles from rice straw. ACS Sustainable Chem Eng 2:726–734

[30] Kim J, Cho S, Bae T, Lee Y (2014) Enzyme biosensor based on an N-doped activated carbon fiber electrode prepared by a thermal solid-state reaction. Sensor Actuat B-Chem 197:20–27

[31] Hassan MF, Chabot V, Li J, Kim KB, Ricardez-Sandoval L, Yu A (2013) Pyrrolic-structure enriched nitrogen doped graphene for highly efficient next generation supercapacitors. J Mater Chem A 1:2904–2912

[32] Hu Z, Li S, Cheng P, Yu W, Li R, Shao X, Lin W, Yuan D (2016) N, P-co-doped carbon nanowires prepared from bacterial cellulose for supercapacitor. J Mater Sci 51:2627–2633

[33] Taer E, Deraman M, Talib IA, Awitdrus A, Hashmi SA, Umar AA (2011) Preparation of a highly porous binderless activated carbon monolith from rubber wood sawdust by a multi-step activation process for application in supercapacitors. Int J Electrochem Sc 6:3301–3315